

Physics-based optimization of Landau parameters for ferroelectrics: application to BZT-50BCT

O A Torres-Matheus¹, R E García² and C M Bishop¹

¹ Department of Mechanical Engineering, University of Canterbury, Private Bag 4800, Christchurch, 8140 New Zealand

² School of Materials Engineering, Purdue University, West Lafayette, IN 47907, USA

E-mail: catherine.bishop@canterbury.ac.nz

3 August 2021

Abstract. In analogy to thermochemical parameter optimization in the CALculation of PHase Diagrams (CALPHAD) approach that relies on a wide variety of experimental measurements, a thermodynamic parameter optimization strategy to describe the polarization response with single-crystal Landau coefficients is documented herein to bridge the gap between CALPHAD, Landau theory and the generality of phase field theory. As an example, anisotropic Landau coefficients are obtained by starting from experimental parameters for Pb-free $0.5\text{Ba}(\text{Zr}_{0.2}\text{Ti}_{0.8})\text{O}_3-0.5(\text{Ba}_{0.7}\text{Ca}_{0.3})\text{TiO}_3$ (BZT-50BCT). Thermodynamic parameters are optimized separately for the rhombohedral (R) and tetragonal (T) ferroelectric phases using a combination of single-crystal and polycrystalline polarization and permittivity data. Parameters are validated against dielectric permittivity as a function of temperature from single-crystal and polycrystalline samples. The optimized parameters correctly predict the sequence of phase transitions as a function of temperature and the paraelectric-ferroelectric transition at 355.5 K is within the experimentally reported range. An upper thermodynamic limit is predicted for R + T metastable coexistence at 302.3 K in agreement with the experimentally measured transition to a stable single T phase for this chemistry at 302 K. The detailed parameter optimization procedure enables the identification of single-crystal tensor properties from experimental measurements for a wide variety of chemistries.

Keywords: Ferroelectric, parameter optimization, Landau coefficients, BZT- x BCT, phase field model

Institute of Physics Publishing *Modelling Simul. Mater. Sci. Eng.*

1. Introduction

Ferroelectric (FE) materials are extensively used in essential dielectric and piezoelectric applications [1]. Recent research on Pb-free and Pb-containing systems has focused on the region of phase space near FE-FE (interferroelectric) transitions, where two FE phases coexist and functional properties are enhanced [2,3]. An interferroelectric phase boundary can be either a compositionally-driven morphotropic phase boundary (MPB) or a temperature-driven polymorphic phase boundary (PPB) [4, 5].

1.1. Models for Ferroelectric Crystals

Traditionally, the selected regions of interest have been analyzed using phenomenological approaches that rely on a single Landau-Devonshire thermodynamic potential, see *e.g.*, [6–9]. For systems with more than one FE phase, all Landau coefficients were fitted to properties from specific FE phases sequentially based on symmetry arguments. Despite significant progress, using a unique set of Landau coefficients to describe more than one FE phase inherently limits the accuracy of predicted properties in the bulk phases and, particularly, near interferroelectric transitions, see *e.g.*, [10–12]. Hence, the structural states and mechanisms responsible for the enhanced response in the vicinity of interferroelectric phase boundaries have not been appropriately examined. Further, as compared to the description of thermochemical systems, where each phase is associated to a unique Gibbs energy state function, the ferroelectrics community has aimed to describe multiple phases with a single free energy state function, even though the historical intent of the Landau expansion was to describe the physics of the material in the vicinity of the paraelectric-ferroelectric (P-FE) phase transition [13].

We proposed a novel multi-phase field model for ferroelectric materials, known as FE-MPF model, to study systems with PPBs [14, 15]. This model couples the Landau-Devonshire thermodynamic potentials of the coexisting FE phases, each defined separately with its own set of Landau coefficients. Since the properties of the FE phases are allowed to vary independently, the FE-MPF model enables a thermodynamically-consistent description of the bulk phases and interferroelectric transitions, and is amenable to being easily extended into multiple-phase descriptions in a way that is consistent with the well established CALculation of PHase Diagrams (CALPHAD) approach.

1.2. Examples of Landau Parameterization from Literature

In either treatment, the free energy is parameterized into physically meaningful and experimentally validated descriptions that enable the equilibrium and kinetic design of ferroelectric materials. For example, Chen summarized Landau coefficients for various systems in an Appendix [16], but a validated set of parameters for common materials or a standard formalism to optimize parameters is missing. Further, the optimization methods, actual experimental data sets and validation data sets are inconsistent and

infrequently reported. Both microstructurally-averaged, polycrystalline and single-crystal Landau coefficients are derived, but must be interpreted carefully.

Polycrystalline Landau coefficients are used for modelling microstructurally-averaged behaviors. Tan *et al.* [17] obtained polycrystalline Landau coefficients for $\text{Pb}_{0.99}\text{Nb}_{0.02}[(\text{Zr}_{0.57}\text{Sn}_{0.43})_{0.94}\text{Ti}_{0.06}]_{0.98}\text{O}_3$, but only stated that parameter values that qualitatively agreed with experimental data were selected and reported no optimization methodology. Zhao *et al.* [18] reported the polycrystalline Landau coefficients for La-doped $\text{Pb}(\text{Zr},\text{Ti})\text{O}_3$ (PZT) and $\text{Bi}_{0.5}\text{Na}_{0.5}\text{TiO}_3 - \text{BaTiO}_3 - \text{K}_{0.5}\text{Na}_{0.5}\text{NbO}_3$ as a function of stress by finding the parameters for a unipolar Landau free energy that exactly solved relations between experimentally measurable quantities in ceramics and the Landau coefficients.

Single-crystal Landau coefficients for various chemistries with interferroelectric transitions have been reported in the literature, but methodologies are not specified. Liang *et al.* [10] determined the Landau coefficients for KNbO_3 over a temperature range including the two interferroelectric transitions using sequential fitting of parameters and validation with experimental methods. While no details on the optimization method were reported, the authors did address the range of reported properties as obtained from different experimental techniques. Zhang *et al.* [19, 20] determined the Landau coefficients for $0.70\text{Pb}(\text{Mg}_{1/3}\text{Nb}_{2/3})\text{O}_3 - 0.30\text{PbTiO}_3$ over a temperature range including an interferroelectric transition and validated them against experimental lattice parameters. They sequentially fitted parameters against the stable part of measured hysteresis loops and performed least squares fitting for other parameters, but data on crystals with slightly different compositions was pooled. Heitmann and Rossetti [21] parameterized BaTiO_3 using isotropic and anisotropic Landau expansion descriptions, fitted to obtain correct first-order interferroelectric transition temperatures and validated against experimental single-crystal lattice parameters. In a follow-up paper, the same authors [6] summarized the thermodynamic models for materials with interferroelectric transitions and provided an overview of the method to sequentially fit temperature- and composition-dependent parameters based on the symmetry of coupled FE phases. However, even though stability requirements and phase diagrams were used to obtain single-crystal Landau coefficients, the detailed parameter optimization methods were not reported.

Pitike *et al.* [22] parameterized a single Landau-Devonshire potential for PbTiO_3 over a temperature range including interferroelectric transitions directly from density functional theory calculations using least squares methods with the requirement of a first order P-FE transition on the Landau parameters. But the predicted interferroelectric transitions were not evaluated or discussed. In contrast, Abolhasani *et al.* [23] used a genetic algorithm to optimize unipolar, microstructurally-averaged Landau coefficients for a poly(vinylidene fluoride) (PVDF) nanocomposite, but the details of the method were not given. Whether the PVDF nanocomposite is a true ferroelectric was disputed by Huang and coworkers [24], who demonstrated that machine learning methods could be used to identify ferroelectric P–E hysteresis loops based on the underlying data sets.

1.3. Lessons from CALPHAD Approach to Parameter Optimization

In this context, parallels to the well-known CALPHAD method are evident [25]. The success of the CALPHAD method hinges on validated databases of parameters for thermodynamic potentials based on a wide-variety of well-documented compound and solution models. The Redlich-Kister polynomial and the sublattice formalisms for excess Gibbs energy are the most common approaches for thermochemical solutions, while the Landau polynomial expansion is the most widely used theoretical construct to describe ferroelectrics. The validated CALPHAD thermochemical parameters are optimized primarily using experimental data including equilibrium phase stability and properties, as are Landau parameters.

However, the thermochemical Gibbs energy is a function of scalar fields (composition, temperature, *etc.*), while the ferroelectric Gibbs energy is a function of vector fields (polarization). For ferroelectric systems, grain size [26] and texture [27] are important due to the vectorial nature of the polarization order parameter and the desire to obtain the anisotropic, single-crystal Landau parameters. While CALPHAD parameter optimization is usually a least squares minimization process that accounts for the accuracy of the experimental measurements [28], a variety of parameter identification methods, usually described as “parameter fitting”, have been reported in the ferroelectric literature, often with few specifics.

Dovbenko *et al.* [29] emphasized the importance of evaluating the accuracy and reliability of experimental measurements. They highlighted the importance of drawing from multiple experimental methods to characterize phase equilibria and using lower order systems to validate higher order predictions, *e.g.*, ternary model parameters should be validated by comparing their predictions for binary end-members against binary experimental data. Further, Kroupa [30] advised using a variety of experimental data, including phase relations and thermodynamic measurements such as enthalpies of mixing and heat capacities, because thermochemical parameter optimization based only on phase stabilities can lead to different sets of “optimized” parameters that each predict the correct phase relations but yield a variety of thermodynamic properties. Moreover, Schmidt-Fetzer *et al.* [31] emphasized the importance of documenting the experimental data and the optimization process for future critical re-assessments.

The CALPHAD extension to ferroelectric modelling highlights experimental challenges, such as volatilization of TiO_2 in BaTiO_3 -based FEs and segregation of elements during high temperature synthesis [32, 33] that can induce large variations in the desired stoichiometry. Electromechanical properties of ceramics vary considerably depending on raw materials, processing, measurement techniques and poling conditions [4, 5]. Acosta *et al.* [4] cautioned that experimental procedures are not well detailed in many ferroelectric research papers and that the importance of some of these conditions is often overlooked.

1.4. BZT- x BCT

Specifically, in Pb-free BaTiO₃-based electroceramics, the $(1 - x)\text{Ba}(\text{Zr}_{0.2}\text{Ti}_{0.8})\text{O}_3 - x(\text{Ba}_{0.7}\text{Ca}_{0.3})\text{TiO}_3$ (BZT- x BCT) system has attracted significant research attention, even though phase stability around its PPB is debated, grey region in Figure 1. While a fraction of the scientific literature supports the hypothesis that the tetragonal (T) and rhombohedral (R) phases coexist at the phase boundary [34–39], other authors suggest that there is an intervening orthorhombic (O) phase and two PPBs [40–44].

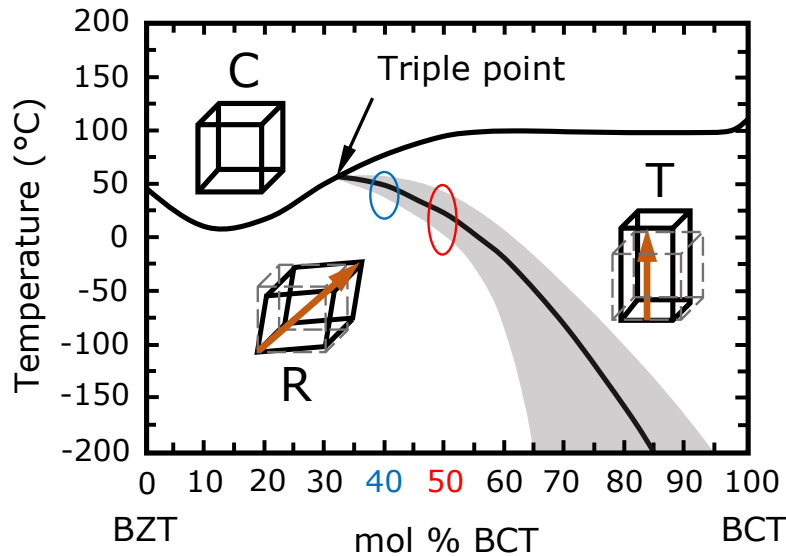


Figure 1. BZT- x BCT pseudo-binary phase diagram, adapted from Torres-Matheus *et al.* [14]. The grey area indicates the experimentally determined region of R+T metastable coexistence (reported elsewhere as an intervening O phase). The region ringed in blue at the BZT-40BCT composition was studied using a coarse-grained approach in previous work [14,15]. Here, single-crystal Landau parameters are obtained for the BZT-50BCT composition to investigate the region of interest near the PPB, ringed in red.

In previous work, we reported the parameterization of 1D and 2D Landau expansions for microstructurally-averaged BZT-40BCT in the FE-MPF model by weighted linear least squares optimization of the P–E experimental data from polycrystals in the unambiguously single phase regions [14, 15]. Parameters were validated by comparison of simulated hysteresis loops in the disputed interferroelectric region of the phase diagram, ringed in blue on Figure 1, to experimental measurements. All experimental data for optimization and validation were from the same source experiments [45], and the optimization methodology was given. Analysis supported R+T coexistence near the PPB.

The most commonly studied composition is BZT-50BCT, also known as $(\text{Ba}_{0.85}\text{Ca}_{0.15})(\text{Zr}_{0.1}\text{Ti}_{0.9})\text{O}_3$ or $0.5\text{Ba}(\text{Zr}_{0.2}\text{Ti}_{0.8})\text{O}_3 - 0.5(\text{Ba}_{0.7}\text{Ca}_{0.3})\text{TiO}_3$, but no single-crystal Landau parameters derived from experiments on BZT-50BCT were found in

the literature. Recently, Yang *et al.* [46] reported single-crystal Landau parameters for BZT- x BCT as a function of temperature and composition (x), and similarly, Zhou *et al.* [47] reported single-crystal Landau parameters for the $(1-x)\text{Ba}(\text{Zr}_{0.2}\text{Ti}_{0.8})\text{O}_3-x(\text{Ba}_{1-y}\text{Ca}_y)\text{TiO}_3$ system (BZT- $x\text{BC}_y\text{T}$) as a function of temperature and compositions (x and y). However, in each study, the coefficients of a single sixth-order Landau-Devonshire potential were obtained by modifying the Landau parameters for pure BaTiO_3 to obtain phase stabilities consistent with published transition temperatures, an approach cautioned against for CALPHAD [30]. Neither paper provided details on the procedures and some measurements on polycrystalline samples were used.

There is a scarcity of single-crystal experimental data for BZT- x BCT. A recent review of Pb-free ferroelectrics grown by solid state processing highlights the difficulties of making single crystals and does not list single crystals for BZT- x BCT [48]. Composition control in liquid growth methods is notoriously hard. For example, while aiming to achieve BZT-50BCT using the flux method, Liu *et al.* [49] obtained an average composition of $\text{Ba}_{0.798}\text{Ca}_{0.202}\text{Zr}_{0.006}\text{Ti}_{0.994}\text{O}_3$ (from energy dispersive spectroscopy), while Sun *et al.* [50] obtained $\text{Ba}_{0.9819}\text{Ca}_{0.0181}\text{Zr}_{0.0004}\text{Ti}_{0.9996}\text{O}_3$ (from inductively coupled plasma mass spectrometry). The closest single crystal to BZT-50BCT was reported by Benabdallah *et al.* [51] with composition $(\text{Ba}_{0.838}\text{Ca}_{0.162})(\text{Ti}_{0.854}\text{Zr}_{0.146})\text{O}_3$ (from electron probe microanalysis).

In this study, we present a general method for optimizing single-crystal Landau coefficients for a ferroelectric with sparse single-crystal experimental data. We document the methodology, including how experimental data from polycrystalline samples is used to estimate single-crystal properties. As an example, we use BZT-50BCT with the FE-MPF model, where each set of Landau coefficients is optimized using data measured in the unambiguously single-phase regions of the phase diagram. Drawing on best practice from the CALPHAD community, we discuss the opportunities for ferroelectric research.

2. Theoretical Model

2.1. Ferroelectric Multi-phase Field Model

The total Helmholtz free energy of a strain-free FE system of volume V , where a polymorphic phase transition occurs at $T = T_{PPB}$ for fixed composition, is defined as [14, 15]

$$F[\vec{P}, \phi; \vec{E}, T] = \int_V \left\{ f(\vec{P}, \phi; \vec{E}, T) + \frac{1}{2} \sum_{k,l=1}^3 \sum_{i,j=1}^3 K_{ijkl} \frac{\partial P_k}{\partial x_i} \frac{\partial P_l}{\partial x_j} + \frac{1}{2} \sum_{i,j=1}^3 K_{ij} \frac{\partial \phi}{\partial x_i} \frac{\partial \phi}{\partial x_j} \right\} dV, \quad (1)$$

where T is the temperature of interest, \vec{E} is the electric field, \vec{P} is the polarization, ϕ is a phase field variable describing the interacting FE phases, $K_{ijkl} = K_P$ is the polarization gradient energy coefficient, and $K_{ij} = K_\phi$ is the phase gradient energy coefficient.

For a system with T and R ferroelectric phases, see Figure 1, the volumetric free energy density in a given grain (crystal) is calculated as

$$f(\vec{P}; \phi; \vec{E}, T) = f_{\text{R}}(\vec{P}; \vec{E}, T)[1 - h(\phi)] + f_{\text{T}}(\vec{P}; \vec{E}, T)h(\phi) + Wg(\phi), \quad (2)$$

where $\phi = 0$ corresponds to the R phase and $\phi = 1$ corresponds to the T phase; $h(\phi) = \phi^3(6\phi^2 - 15\phi + 10)$ is a function that interpolates between the free energy densities of the two phases, f_{R} and f_{T} ; $g(\phi) = \phi^2(1 - \phi)^2$ is a double-well potential that prevents unphysical phase transitions; and W is the double-well coefficient that controls the height of the energy barrier between FE phases. The individual homogeneous free energy densities are defined herein as

$$f_{\text{T}}(\vec{P}; \vec{E}, T) = f_{\text{T}}^{\circ}(\vec{P}; \vec{E}, T), \quad (3a)$$

$$f_{\text{R}}(\vec{P}; \vec{E}, T) = f_{\text{R}}^{\circ}(\vec{P}; \vec{E}, T) + \Delta f_{PPB}, \quad (3b)$$

where f_{T}° and f_{R}° are the free energy densities traditionally described by the Helmholtz thermodynamic potential with respect to the cubic (C) paraelectric phase, and $\Delta f_{PPB} = f_{\text{T}}^{\circ}(\vec{P}_{s\text{T}}; \vec{0}, T_{PPB}) - f_{\text{R}}^{\circ}(\vec{P}_{s\text{R}}; \vec{0}, T_{PPB})$, see [14, 15] for full details.

According to Cao [52, 53], the Helmholtz thermodynamic potential up to the sixth-order terms is generally expressed in terms of three polarization components, $\vec{P} = (P_1, P_2, P_3)$, as the following Landau-Devonshire potential

$$\begin{aligned} f^{\circ}(\vec{P}; \vec{E}, T) = & \alpha_1(P_1^2 + P_2^2 + P_3^2) + \alpha_{11}(P_1^4 + P_2^4 + P_3^4) \\ & + \alpha_{12}(P_1^2 P_2^2 + P_2^2 P_3^2 + P_1^2 P_3^2) + \alpha_{111}(P_1^6 + P_2^6 + P_3^6) \\ & + \alpha_{112} [P_1^4(P_2^2 + P_3^2) + P_2^4(P_1^2 + P_3^2) + P_3^4(P_1^2 + P_2^2)] \\ & + \alpha_{123} P_1^2 P_2^2 P_3^2 - P_1 E_1 - P_2 E_2 - P_3 E_3, \end{aligned} \quad (4)$$

where the leading coefficient is commonly defined as $\alpha_1 = \alpha_{CW}(T - T_{CW})$, where T_{CW} is the Curie-Weiss temperature and $\alpha_{CW} > 0$ is the Curie-Weiss constant; while the other expansion parameters are considered temperature-independent [54]. This is the simplest polynomial expansion that stabilizes R and T phase symmetries. For first order paraelectric-ferroelectric transitions, the Curie temperature is $T_C = T_{CW} + 3(\alpha_{11} + \alpha_{12})^2 / [4\alpha_{CW}(3\alpha_{111} + 6\alpha_{112} + \alpha_{123})]$, and the maximum temperature limit of metastability of the ferroelectric phase is $T_{max} = T_{CW} + (\alpha_{11} + \alpha_{12})^2 / [\alpha_{CW}(3\alpha_{111} + 6\alpha_{112} + \alpha_{123})]$.

The allowed domain states, or variants, for each FE phase depend on its crystal structure. For the T phase, polarizations are along the $\langle 100 \rangle$ directions of the local pseudocubic axes with coordinates $[x_1, x_2, x_3]$; while for the R phase, polarizations are along the pseudocubic $\langle 111 \rangle$ family of directions. Considering the case of $\vec{P}_{\text{T}} = (0, 0, P_3)$ and $\vec{P}_{\text{R}} = (P_3, P_3, P_3)$ in the absence of an applied electric field ($\vec{E} = \vec{0}$), the volumetric free energy densities f_{T}° and f_{R}° are obtained from (4) as

$$f_{\text{T}}^{\circ}(\vec{P}_{\text{T}}; T) = \alpha_{1,\text{T}} P_3^2 + \alpha_{11,\text{T}} P_3^4 + \alpha_{111,\text{T}} P_3^6, \quad (5a)$$

$$\begin{aligned} f_{\text{R}}^{\circ}(\vec{P}_{\text{R}}; T) = & 3\alpha_{1,\text{R}} P_3^2 + 3(\alpha_{11,\text{R}} + \alpha_{12,\text{R}}) P_3^4 \\ & + (3\alpha_{111,\text{R}} + 6\alpha_{112,\text{R}} + \alpha_{123,\text{R}}) P_3^6, \end{aligned} \quad (5b)$$

where subscripts T and R are used to denote the set of Landau coefficients in the T and R phases. Further, the equilibrium states are obtained from the minimization of

(4) and substitution of the allowed solutions for polarization in each phase, *i.e.*,

$$\left. \frac{\partial f_{\text{T}}^{\circ}(\vec{P}; T)}{\partial P_3} \right|_{\vec{P}=\vec{P}_{s,\text{T}}} = \alpha_{1,\text{T}} + 2\alpha_{11,\text{T}}P_{s3,\text{T}}^2 + 3\alpha_{111,\text{T}}P_{s3,\text{T}}^4 = 0, \quad (6a)$$

$$\begin{aligned} \left. \frac{\partial f_{\text{R}}^{\circ}(\vec{P}; T)}{\partial P_3} \right|_{\vec{P}=\vec{P}_{s,\text{R}}} &= \alpha_{1,\text{R}} + 2(\alpha_{11,\text{R}} + \alpha_{12,\text{R}})P_{s3,\text{R}}^2 \\ &+ (3\alpha_{111,\text{R}} + 6\alpha_{112,\text{R}} + \alpha_{123,\text{R}})P_{s3,\text{R}}^4 = 0, \end{aligned} \quad (6b)$$

where P_{s3} is the component of the spontaneous polarization that stabilizes the system in the absence of applied electric fields. The spontaneous polarization is defined as $\|\vec{P}_{s,\text{T}}\| = P_{s3,\text{T}}$ for the T phase and $\|\vec{P}_{s,\text{R}}\| = \sqrt{3}P_{s3,\text{R}}$ for the R phase, and its magnitude is obtained from (6a) and (6b) as

$$P_{s3,\text{T}} = \pm \left[\frac{-\alpha_{11,\text{T}} + \sqrt{\alpha_{11,\text{T}}^2 - 3\alpha_{1,\text{T}}\alpha_{111,\text{T}}}}{3\alpha_{111,\text{T}}} \right]^{1/2}, \quad (7a)$$

$$\begin{aligned} P_{s3,\text{R}} = \pm &\left[\frac{-(\alpha_{11,\text{R}} + \alpha_{12,\text{R}})}{3\alpha_{111,\text{R}} + 6\alpha_{112,\text{R}} + \alpha_{123,\text{R}}} \right. \\ &\left. + \frac{\sqrt{(\alpha_{11,\text{R}} + \alpha_{12,\text{R}})^2 - \alpha_{1,\text{R}}(3\alpha_{111,\text{R}} + 6\alpha_{112,\text{R}} + \alpha_{123,\text{R}})}}{3\alpha_{111,\text{R}} + 6\alpha_{112,\text{R}} + \alpha_{123,\text{R}}} \right]^{1/2}. \end{aligned} \quad (7b)$$

Similarly, the longitudinal and transverse components of the dielectric permittivity are determined from the second partial derivatives of (4), *i.e.*,

$$\begin{aligned} \frac{\partial^2 f^{\circ}}{\partial P_3^2} = \frac{\partial E_3}{\partial P_3} = \frac{1}{\epsilon_{33}} &= 2\alpha_1 + 12\alpha_{11}P_3^2 + 2\alpha_{12}(P_1^2 + P_2^2) + 30\alpha_{111}P_3^4 \\ &+ 2\alpha_{112}[P_1^4 + P_2^4 + 6P_3^2(P_1^2 + P_2^2)] + 2\alpha_{123}P_1^2P_2^2, \end{aligned} \quad (8a)$$

$$\begin{aligned} \frac{\partial^2 f^{\circ}}{\partial P_1^2} = \frac{\partial E_1}{\partial P_1} = \frac{1}{\epsilon_{11}} &= 2\alpha_1 + 12\alpha_{11}P_1^2 + 2\alpha_{12}(P_2^2 + P_3^2) + 30\alpha_{111}P_1^4 \\ &+ 2\alpha_{112}[P_2^4 + P_3^4 + 6P_1^2(P_2^2 + P_3^2)] + 2\alpha_{123}P_2^2P_3^2, \end{aligned} \quad (8b)$$

$$\frac{\partial^2 f^{\circ}}{\partial P_1 \partial P_2} = \frac{\partial E_1}{\partial P_2} = \frac{1}{\epsilon_{12}} = 4\alpha_{12}P_1P_2 + 8\alpha_{112}(P_1P_2^3 + P_1^3P_2) + 4\alpha_{123}P_1P_2P_3^2. \quad (8c)$$

Note that similar expressions can be written for ϵ_{22} , ϵ_{23} and ϵ_{31} . Based on the condition of zero applied field, (8a) through (8c) can be simplified by substituting the spontaneous polarization of each phase. Hence,

For the T phase: [55]

$$\epsilon_{33,\text{T}} = (2\alpha_{1,\text{T}} + 12\alpha_{11,\text{T}}P_{s3,\text{T}}^2 + 30\alpha_{111,\text{T}}P_{s3,\text{T}}^4)^{-1}, \quad (9a)$$

$$\epsilon_{11,\text{T}} = \epsilon_{22,\text{T}} = (2\alpha_{1,\text{T}} + 2\alpha_{12,\text{T}}P_{s3,\text{T}}^2 + 2\alpha_{112,\text{T}}P_{s3,\text{T}}^4)^{-1}, \quad (9b)$$

$$\epsilon_{12,\text{T}} = \epsilon_{23,\text{T}} = \epsilon_{31,\text{T}} = 0. \quad (9c)$$

For the R phase: [56]

$$\begin{aligned} \epsilon_{33,\text{R}} = \epsilon_{22,\text{R}} = \epsilon_{11,\text{R}} &= [2\alpha_{1,\text{R}} + (12\alpha_{11,\text{R}} + 4\alpha_{12,\text{R}})P_{s3,\text{R}}^2 \\ &+ (30\alpha_{111,\text{R}} + 28\alpha_{112,\text{R}} + 2\alpha_{123,\text{R}})P_{s3,\text{R}}^4]^{-1}, \end{aligned} \quad (10a)$$

$$\epsilon_{12,\text{R}} = \epsilon_{23,\text{R}} = \epsilon_{31,\text{R}} = [4\alpha_{12,\text{R}}P_{s3,\text{R}}^2 + (16\alpha_{112,\text{R}} + 4\alpha_{123,\text{R}})P_{s3,\text{R}}^4]^{-1}. \quad (10b)$$

Alternatively, the dielectric permittivity in the R phase can be expressed using a new local coordinate system such that the x_3 axis is parallel to the [111] direction. Expressing (10a) and (10b) in the new local coordinate system $[x'_1, x'_2, x'_3]$ results in a diagonal matrix, similar to that obtained for the T phase, with the following elements [10, 11]

$$\epsilon'_{33,R} = \epsilon_{11,R} + 2\epsilon_{12,R}, \quad (11a)$$

$$\epsilon'_{11,R} = \epsilon'_{22,R} = \epsilon_{11,R} - \epsilon_{12,R}, \quad (11b)$$

$$\epsilon'_{12,R} = \epsilon'_{23,R} = \epsilon'_{31,R} = 0. \quad (11c)$$

2.2. Intrinsic Properties of Ferroelectric Ceramics

The properties of FE ceramics consist of two contributions: intrinsic, which originate from lattice dynamics and are equivalent to properties obtained from a single domain; and extrinsic, which represent non-lattice contributions and arise mainly from changes at domain walls and grain boundaries [57, 58]. Further, poled FE ceramics with randomly oriented grains are transversely isotropic around the poling axis regardless of the crystal symmetry [58–60]. Hence, for a polycrystalline sample described by global coordinates $[X_1, X_2, X_3]$ with an electric field applied along the global $[0, 0, 1]$ direction, the resulting through-thickness polarization and dielectric permittivity have the same non-zero elements as crystals that belong to point group $6mm$, *i.e.*, [59, 61]

$$\vec{P} = \begin{pmatrix} 0 \\ 0 \\ P_3 \end{pmatrix}, \quad \vec{\epsilon} = \begin{pmatrix} \epsilon_{11} & 0 & 0 \\ 0 & \epsilon_{11} & 0 \\ 0 & 0 & \epsilon_{33} \end{pmatrix}. \quad (12)$$

The intrinsic properties given by Equation (12) depend on, and are limited by, the allowed polarization directions associated with the crystal symmetry of the FE phase(s) [59]. The maximum achievable properties of FE ceramics in a saturated poling state have been estimated from single-crystal data via probability density functions of orientation (PDFOs) [57], pole figures [62], inverse pole figures [63] and/or orientation distribution function (ODF) [60, 64, 65] methods. In these models, macroscopic properties are estimated as the averaged response of randomly oriented grains over the entire orientation space. A Reuss type approximation [66] is commonly adopted, which neglects the interaction between crystals by assuming that domains are independent of each other and that the internal and external electromechanical loadings are equal.

For the T and R phases, the saturated remnant polarization of FE ceramics, P_r^* , can be estimated from the magnitude of the spontaneous polarization in the single crystal as [57, 59, 60, 62–65]

$$P_{rT}^* = 0.8312P_{sT}, \quad (13a)$$

$$P_{rR}^* = 0.8660P_{sR}. \quad (13b)$$

Similarly, the saturated macroscopic dielectric permittivities along the polarization

direction, ϵ_{33}^* , and in the transverse direction, ϵ_{11}^* , are [57, 60]

$$\begin{bmatrix} \epsilon_{11,T}^* \\ \epsilon_{33,T}^* \end{bmatrix} = \frac{1}{3\pi} \begin{bmatrix} 2\pi + \sqrt{3} & \pi - \sqrt{3} \\ 2\pi - 2\sqrt{3} & \pi + 2\sqrt{3} \end{bmatrix} \begin{bmatrix} \epsilon_{11,T} \\ \epsilon_{33,T} \end{bmatrix}, \quad (14a)$$

$$\begin{bmatrix} \epsilon_{11,R}^* \\ \epsilon_{33,R}^* \end{bmatrix} = \frac{1}{3\pi} \begin{bmatrix} 2\pi + 2 & \pi - 2 \\ 2\pi - 4 & \pi + 4 \end{bmatrix} \begin{bmatrix} \epsilon'_{11,R} \\ \epsilon'_{33,R} \end{bmatrix}, \quad (14b)$$

where ϵ_{33} (ϵ'_{33}) and ϵ_{11} (ϵ'_{11}) are the longitudinal and transverse permittivity components in a single FE domain [57]. These solutions, which assume a fully saturated poling state, are ideal and provide an upper limit to the properties of polycrystalline ferroelectrics [58, 60]. However, FE ceramics rarely reach a fully poled state [57, 59, 65]. Many domains cannot reorient along available polarization directions due to internal fields associated with grain boundaries, and some domains will switch back after removal of the poling field [59].

Hou *et al.* [57] developed a model for unsaturated poling states by incorporating additional parameters into the PDFOs to account for the remnant switching fraction of different types of domain switching, which can be determined using X-ray diffraction (XRD). Thus, the remnant polarization in an unsaturated state, P_r^{**} , is given by

$$P_{rT}^{**} = \left(1 - \frac{1}{3}t_{180} - \frac{2}{3}t_{90}\right) 0.8312P_{sT}, \quad (15a)$$

$$\begin{aligned} P_{rR}^{**} &= \left(1 - \frac{3}{8}r_{71} - \frac{3}{8}r_{109} - \frac{1}{4}r_{180}\right) 0.8660P_{sR} \\ &\quad + \frac{\sqrt{3}}{16}(r_{71} - r_{109})P_{sR}, \end{aligned} \quad (15b)$$

where t_{90} and t_{180} are the remnant fractions of 90° and 180° switching in the T phase; and r_{71} , r_{109} and r_{180} are the remnant fractions of 71°, 109° and 180° switching in the R phase. When all the remnant switching fractions are zero, (15a) and (15b) reduce to the saturated poling state; and when all the remnant switching fractions are one, the equations reduce to the randomly-oriented initial state. Similarly, the dielectric permittivity components under unsaturated poling state, ϵ_{33}^{**} and ϵ_{11}^{**} , can be calculated as [57]

$$\begin{aligned} \begin{bmatrix} \epsilon_{11,T}^{**} \\ \epsilon_{33,T}^{**} \end{bmatrix} &= \frac{1}{3\pi} \begin{bmatrix} 2\pi + \sqrt{3} & \pi - \sqrt{3} \\ 2\pi - 2\sqrt{3} & \pi + 2\sqrt{3} \end{bmatrix} \begin{bmatrix} \epsilon_{11,T} \\ \epsilon_{33,T} \end{bmatrix} \\ &\quad + \frac{t_{90}}{3\pi} \begin{bmatrix} -\sqrt{3} & \sqrt{3} \\ 2\sqrt{3} & -2\sqrt{3} \end{bmatrix} \begin{bmatrix} \epsilon_{11,T} \\ \epsilon_{33,T} \end{bmatrix}, \end{aligned} \quad (16a)$$

$$\begin{aligned} \begin{bmatrix} \epsilon_{11,R}^{**} \\ \epsilon_{33,R}^{**} \end{bmatrix} &= \frac{1}{3\pi} \begin{bmatrix} 2\pi + 2 & \pi - 2 \\ 2\pi - 4 & \pi + 4 \end{bmatrix} \begin{bmatrix} \epsilon'_{11,R} \\ \epsilon'_{33,R} \end{bmatrix} \\ &\quad + \frac{r_{71} + r_{109}}{3\pi} \begin{bmatrix} -1 & 1 \\ 2 & -2 \end{bmatrix} \begin{bmatrix} \epsilon'_{11,R} \\ \epsilon'_{33,R} \end{bmatrix}. \end{aligned} \quad (16b)$$

According to Yang *et al.* [65], 180° domain switching can readily reach saturation in FE ceramics, while other switching types do not, resulting in switching fractions as

low as 44% in PZT. This result agrees with computational simulations performed by Li *et al.* [67], who reported little domain texture for tetragonal PZT due to a small fraction of 90° domain switching.

3. Parameter Optimization Procedure: Application to BZT-50BCT

The following procedure to determine the Landau parameters for the R and T phases of the BZT-50BCT system used a combination of experimental data from single-crystal and polycrystalline samples reported in the literature. The single-crystal data were taken from Benabdallah *et al.* [51], who successfully grew a single-crystal with composition $(\text{Ba}_{0.838}\text{Ca}_{0.162})(\text{Zr}_{0.146}\text{Ti}_{0.854})\text{O}_3$, close to the intended stoichiometry for BZT-50BCT. Experimental data include the spontaneous polarization and dielectric permittivity measured in the pseudocubic [001] direction over temperatures 150 K to 375 K. The authors reported anomalies in the permittivity measurements at 265 K and 366 K, consistent with transition temperatures measured for the BZT-50BCT system. In particular, the cubic-tetragonal transition obtained at 366 K is within the 364 ± 13 K range reported by Acosta *et al.* [4].

In the FE-MPF model, the Landau parameters of each FE phase are obtained independently from experimental data measured in the unambiguously T and R regions of the phase diagram. For the BZT- x BCT system, a region of R+T coexistence (or an intervening O phase) has been speculated. In particular, for BZT-50BCT the region in dispute extends from $T_{\text{R-O}} = 274$ K to $T_{\text{O-T}} = 302$ K, according to Ehmke [45]. The coefficients for the R phase were optimized to data measured at $T \leq T_{\text{R-O}}$; and the coefficients for the T phase were optimized to data measured at $T_{\text{O-T}} \leq T \leq T_{\text{T-C}}$, where $T_{\text{T-C}} = 366$ K, as reported by Benabdallah *et al.* [51]. Figure 2 is the flow chart of the parameter optimization procedure used in this study.

For the R phase, all Landau parameters were optimized simultaneously by non-linear least squares fitting of Equation (7b) to P_s vs T single-crystal data from 200 K to 274 K using the `lbfgsb` method from `lmfit` python package [68]. The algorithm was initialized to parameters with the same order of magnitude as the parameters for BaTiO_3 determined by Bell and Cross [69], and bounds were set for each parameter according to the conditions for stability of the R phase as discussed by Smolenskii *et al.* [70]. Data in the 270 K to 274 K range were given a higher weight (probability of approximately 100% set through a σ parameter in `lmfit`) as they are closer to the region of interest where the R and T phases coexist. The default values for tolerances and maximum number of function evaluations were used, 1×10^{-7} and $2000(\text{number_of_variables} + 1)$, respectively. If the algorithm did not converge, the initial estimate and weight factors were adjusted. The goodness of fit was calculated using root mean square error (RMSE). The optimized Landau coefficients for the rhombohedral phase predict a first order P-FE transition and a maximum temperature for metastability of the R phase at $T_{\text{max,R}} = 302.3$ K, which is consistent with the experimentally measured orthorhombic-tetragonal transition at $T_{\text{O-T}} = 302$ K. The

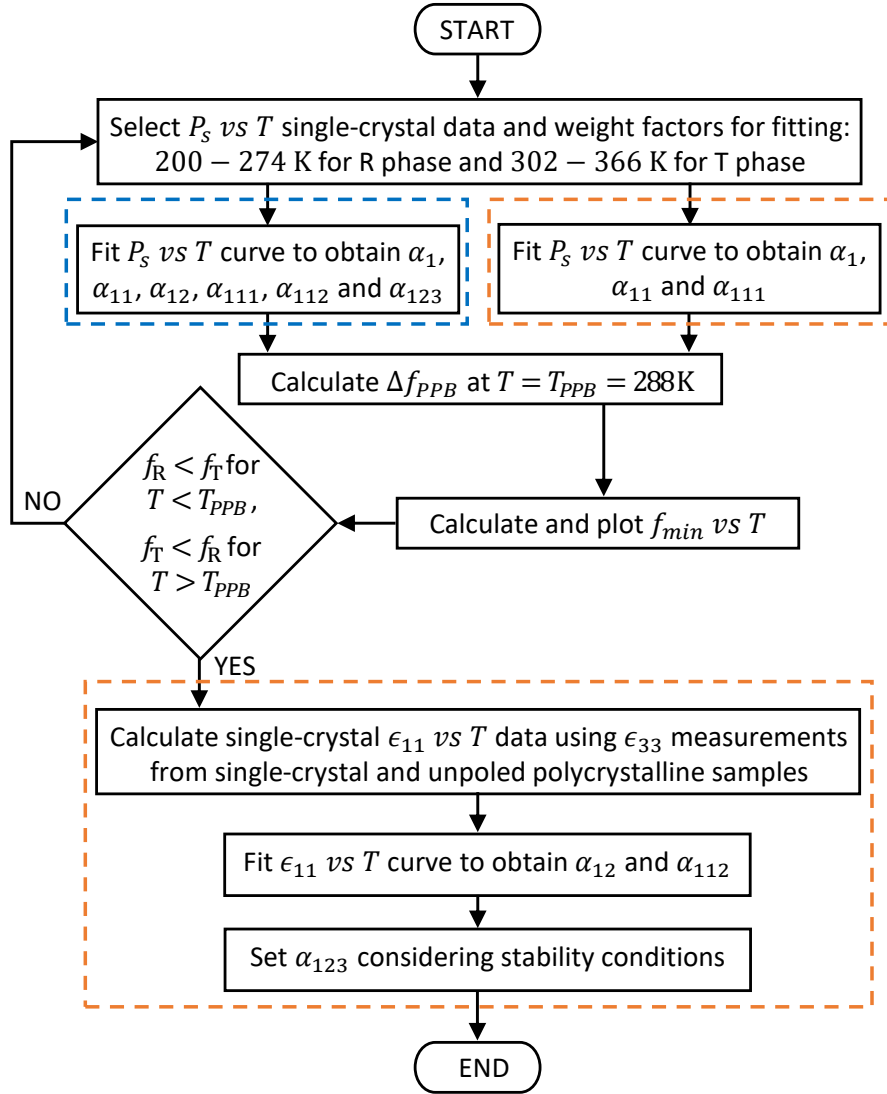


Figure 2. Flow chart of parameter optimization procedure for the anisotropic, single-crystal Landau coefficients for the R (---) and T (---) phases of BZT-50BCT in the FE-MPF model.

predicted temperature represents a thermodynamic upper limit for R+T metastable coexistence and explains the apparent stabilization of an O phase reported near the polymorphic T-R phase boundary. Below the $T_{max,R}$, the estimated Landau coefficients correctly reproduce the R phase, which can exist in a stable or metastable state. Results validate the multi-phase field approach to resolve the PPB in BZT- x BCT.

Similarly, for the T phase, $\alpha_{1,T}$, $\alpha_{11,T}$ and $\alpha_{111,T}$ were optimized simultaneously using the `leastsq` method from `lmfit` for Equation (7a) to P_s vs T single-crystal data from 302 K to 366 K with higher weight given to data at $T \leq 305$ K. Again, the default values for tolerances and maximum number of function evaluations were used, 1×10^{-7} and $2000(\text{number_of_variables} + 1)$, respectively. If the algorithm did not converge, the initial estimate and weight factors were adjusted. The predicted $T_{CW,T} = 355.5$ K is

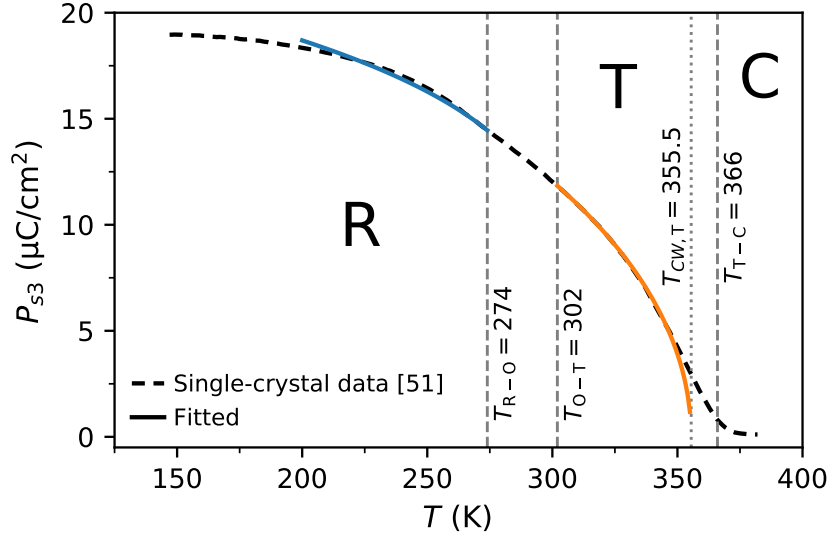


Figure 3. Comparison of predicted Landau parameters for the R (—) and T (—) phases of the BZT-50BCT system to P_s vs T single-crystal data. For the R phase, all the Landau coefficients were obtained using experimental data from 200 K to 274 K. For the T phase, coefficients $\alpha_{1,T}$, $\alpha_{11,T}$ and $\alpha_{111,T}$ were obtained by using experimental data from 302 K to 366 K. The transition temperatures T_{R-O} and T_{O-T} are from Ehmke [45], and T_{T-C} is from Benabdallah *et al.* [51]. A second order P-FE transition is observed for the T phase at its calculated Curie-Weiss temperature, $T_{CW,T}$.

within the 364 ± 13 K range stated by Acosta *et al.* [4].

A sensitivity analysis [15] showed that the specific choice for the PPB temperature does not affect the results from the FE-MPF model. Thus, the PPB temperature was fixed midway between the lower and upper limits for R+T coexistence determined by Ehmke [45], $T_{PPB} = (T_{R-O} + T_{O-T})/2 = 288$ K. The value of Δf_{PPB} was computed using the optimized coefficients, see Figure 2. To confirm that the R phase is globally stable for $T < T_{PPB}$ and the T phase is stable for $T > T_{PPB}$, the minimum volumetric free energy density of each FE phase was calculated by substituting the respective spontaneous polarization, P_{s3} , into Equations (5a) and (5b). The initial estimate and weight factors were adjusted until appropriate coefficients were found for each FE phase.

$\alpha_{12,T}$ and $\alpha_{112,T}$ were optimized to Equation (9b) with estimated single-crystal $\epsilon_{11,T}$ data from 302 K to 355.5 K following [19, 55], Figure 4. In order to reproduce the randomly-oriented domains of the unpoled ceramics, the remnant fraction of 90° switching, t_{90} , was set to one for unsaturated poling. Thus, from Equation (16a)

$$\epsilon_{11,T} = (3\epsilon_{33,T}^{**} - \epsilon_{33,T})/2 \quad (17)$$

where $\epsilon_{33,T}$ is the longitudinal permittivity in the single-crystal sample and $\epsilon_{33,T}^{**}$ is the longitudinal permittivity in the ceramic sample. In Figure 4, a non-linear least squares optimization was performed using `leastsq` method of `lmfit` as described above with two independent variables, T and $P_{s3,T}$ from Benabdallah *et al.* [51]. Different sources were considered for $\epsilon_{33,T}^{**}$ [37, 71–73] until the Landau parameters gave the lowest RMSE for the estimated $\epsilon_{11,T}$ data using [71], with $\alpha_{12,T} > 0$ and $\alpha_{112,T} > 0$. The latter is

required to ensure stabilization of the T phase. Finally, we set $\alpha_{123,T} = 0$, in agreement with Smolenskii *et al.* [70] in order to prevent spontaneous phase transitions to the R or O phases in the entire temperature range of interest.

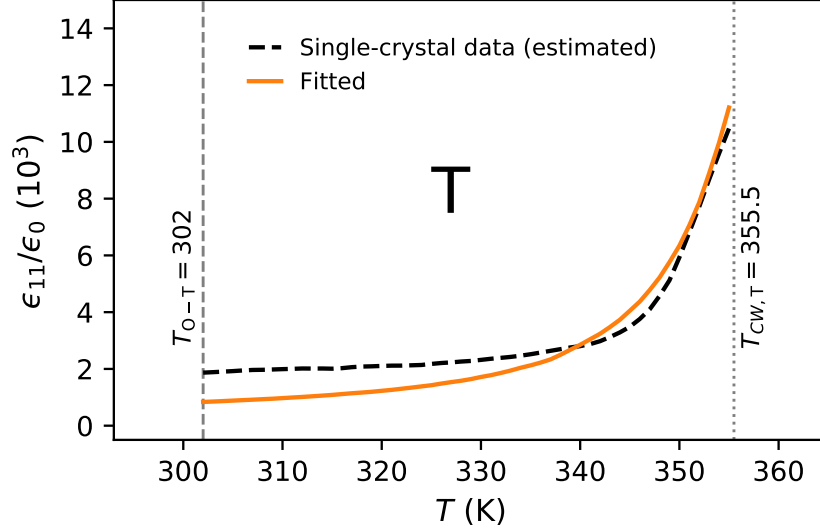


Figure 4. Comparison of predicted ϵ_{11} as a function of temperature for the T phase (—) to estimated single-crystal data, where $\alpha_{12,T}$ and $\alpha_{112,T}$ were optimized parameters. The single-crystal ϵ_{11} data were estimated using ϵ_{33} measurements for a single-crystal sample from Benabdallah *et al.* [51] and for an unpoled polycrystalline sample from Zhang *et al.* [71].

4. Results and Discussion

The BZT-50BCT Landau parameters obtained herein are summarized in Table 1. The T phase has a second order P-FE phase transition and the R phase exhibits a weak first order P-FE transition. The latter is evidenced by the similar values for the Curie-Weiss temperature, $T_{CW,R} = 299.0$ K, the Curie temperature, $T_{C,R} = 301.5$ K, and the maximum temperature for metastability of the rhombohedral phase, $T_{max,R} = 302.3$ K. Table 1 also includes Landau coefficients for a single Landau-Devonshire potential for both FE phases reported in the literature [46, 47]. The Curie temperature reported in those works, $T_C = 353$ K, is approximately equal to the value predicted in this study for the T-C phase transition at $T_{CW,T} = T_{C,T} = 355.5$ K. Further, the Landau parameters reported by all sources exhibit similar order of magnitudes.

Figure 5 shows that at $T = T_{PPB}$, the rhombohedral and tetragonal phases are both stable and coexist. Figure 5(c)-(f) show the three-dimensional free energy surface for a specific FE phase at selected temperatures. For the R phase, Figure 5(c)-(d) confirm that optimized Landau coefficients stabilize polarization states along the $\langle 111 \rangle$ directions, while for the T phase, Figure 5(e)-(f) show that optimized Landau coefficients stabilize polarization states along the $\langle 100 \rangle$ directions.

Table 1. Optimized Landau parameters for the R and T phases of BZT-50BCT. Landau coefficients found in the literature are also included for comparison. The parameters reported by Yang *et al.* [46] have been adapted to the notation used in the present work.

| Symbol | This work | | Yang <i>et al.</i> [46] | Zhou <i>et al.</i> [47] | Units |
|------------------|--------------------------------------|--|--|--|---------------------------------|
| | R phase | T phase | | | |
| α_1 | $1.450 \times 10^5 \times (T - 299)$ | $1.800 \times 10^5 \times (T - 355.5)$ | $2.071 \times 10^5 \times (T - 353)$ | $4.124 \times 10^5 \times (T - 353)$ | Jm/C ² |
| α_{11} | 1.000×10^7 | 3.225×10^8 | $-4.5 \times 10^6 + 1.89 \times 10^5 \times (T - 335)$ | -8.0×10^7 | Jm ⁵ /C ⁴ |
| α_{12} | -1.000×10^8 | 5.501×10^9 | $-4.5 \times 10^6 - 1.89 \times 10^5 \times (T - 335)$ | $2.0 \times 10^7 + 3.0 \times 10^5 \times (T - 343)$ | Jm ⁵ /C ⁴ |
| α_{111} | 3.552×10^9 | 1.000×10^9 | 1.304×10^8 | 1.294×10^9 | Jm ⁹ /C ⁶ |
| α_{112} | -4.582×10^8 | 1.023×10^7 | -5.5×10^6 | -2.0×10^7 | Jm ⁹ /C ⁶ |
| α_{123} | 9.000×10^9 | 0.000 | $2.5 \times 10^9 + 3.5 \times 10^7 \times (T - 335)$ | 8.0×10^7 | Jm ⁹ /C ⁶ |
| Δf_{PPB} | -3.198×10^4 | — | — | — | J/m ³ |

Figure 6 illustrates the thermodynamic conditions for phase coexistence and stability near the PPB in BZT-50BCT. The predicted upper limit for metastable R+T phase coexistence, $T_{max,R} = 302.3$ K, is approximately equal to $T_{O-T} = 302$ K, as reported by Ehmke [45]. Results support the hypothesis of R+T phase coexistence in the vicinity of the PPB [14, 15], and no metastable coexistence between the C phase and the R and T ferroelectric phases is predicted for this composition, in agreement with experimental observations [34].

Figure 7 compares predicted spontaneous polarization component, P_{s3} , and longitudinal relative permittivity, ϵ_{33}/ϵ_o , for single-crystal BZT-50BCT using our optimized Landau coefficients and those reported by Yang *et al.* [46] and Zhou *et al.* [47], summarized in Table 1, with experimental data [51]. Considering the ongoing debate on the structural state in the vicinity of the PPB, comparison of our thermodynamic model predictions to experimental measurements is only made at temperatures in the unambiguously single-phase regions, $T < 274$ K for the rhombohedral phase and $T > 302$ K for the tetragonal phase. Figure 7(a) shows that the new model is in good agreement with single-crystal experimental data across both R and T phases, with RMSE of $0.55 \mu\text{C}/\text{cm}^2$. In comparison, the predictions from the prior published models [46, 47] overestimate and deviate significantly from the experimental data, with RMSE of $41 \mu\text{C}/\text{cm}^2$ and $20 \mu\text{C}/\text{cm}^2$, respectively. In part, this is because those studies were not optimized against any experimental property measurements, but, instead, their Landau parameters were determined by modifying the coefficients of BaTiO₃ to generate

a consistent phase diagram for the BZT- x BCT system. Figure 7(b) shows that the permittivity predicted in this study provides the best agreement with experimental data for the R phase and the T phase near the region of interest. In comparison, previous work by Zhou *et al.* [47] and Yang *et al.* [46] underestimate the permittivity and provide RMSE of 1500 and 2000, respectively, compared to 110 herein. Divergence is evident as $T \rightarrow T_{CW,T}$ for all the permittivity predictions, inset Figure 7(b). For our optimized parameters, this results from the assumptions used in the Landau expansion, including that only the first coefficient, $\alpha_{1,T}$, is a function of temperature, and because

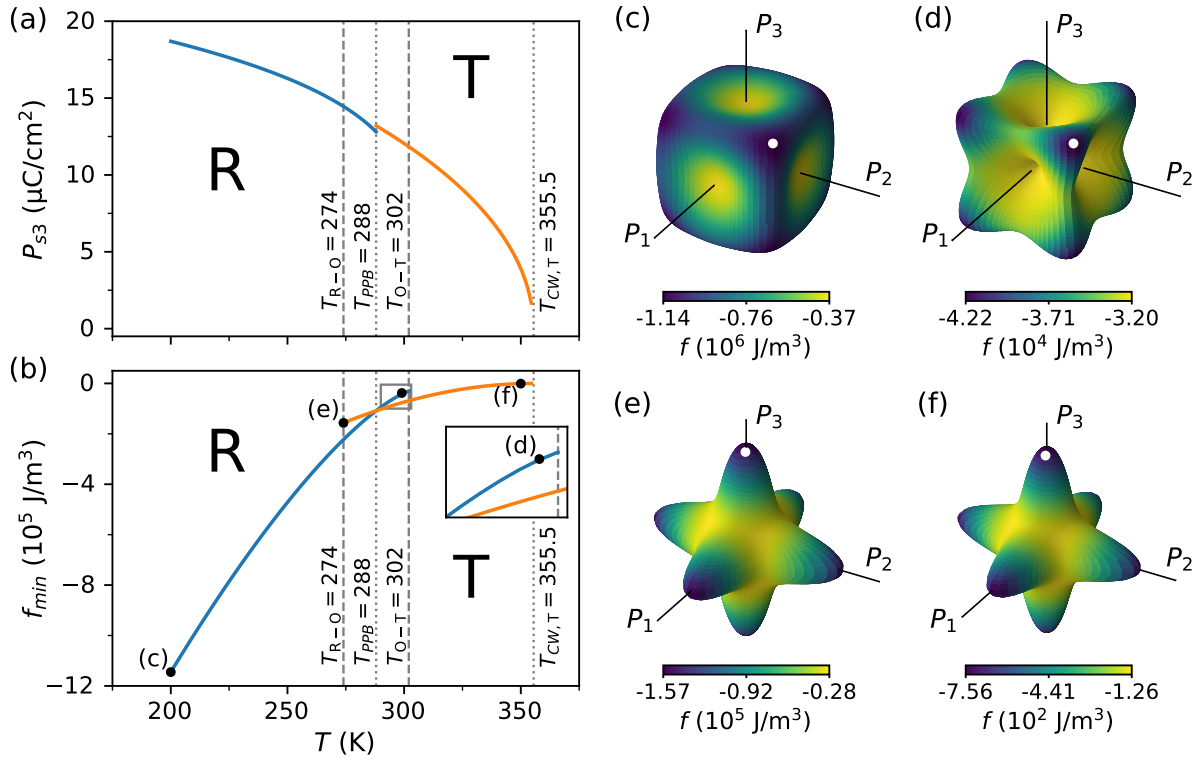


Figure 5. Predicted temperature dependence of (a) spontaneous polarization, P_{s3} , and (b) minimum volumetric free energy density, f_{min} , for the R (—) and T (—) phases of BZT-50BCT. The transition temperatures T_{R-O} and T_{O-T} are from Ehmke [45]. The PPB temperature was taken as $T_{PPB} = (T_{R-O} + T_{O-T})/2$. A second order P-FE transition is observed for the T phase at its calculated Curie-Weiss temperature, $T_{CW,T}$. Inset in (b) corresponds to a magnified view of the area highlighted near the T_{O-T} with state of interest indicated. The volumetric free energy density surface is illustrated in 3-D for (c) stable R phase at $T = 200$ K, (d) metastable R phase at $T = 299$ K, (e) metastable T phase at $T = 274$ K, and (f) stable T phase at $T = 350$ K. For each case, the surface shape is defined by the polarization vector that minimizes the volumetric free energy density at each spatial orientation, and the surface colour map corresponds to the magnitude of that free energy density. A white dot indicates one of the polarization variants corresponding to the spontaneous polarization of that phase. With the optimized Landau coefficients stated in Table 1, $f_{min,R} < f_{min,T}$ for $T < T_{PPB}$ and $f_{min,T} < f_{min,R}$ for $T > T_{PPB}$, confirming the correct global stability predictions.

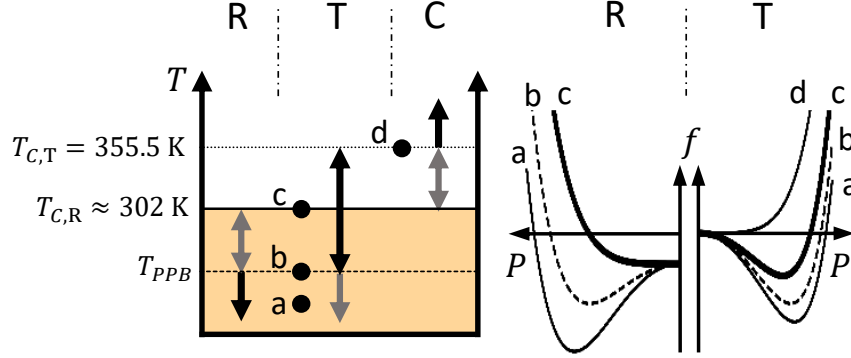


Figure 6. Phase coexistence and stability predictions for the BZT-50BCT system. The T phase has a second order P-FE phase transition, with $T_{C,T} = T_{CW,T}$, above which the cubic (C) phase is globally stable. The R phase has a weak first order P-FE transition, evidenced by $T_{CW,R} \sim T_{C,R} \sim T_{max,R}$. A polymorphic phase transition occurs at T_{PPB} . Highlighted area indicates metastable coexistence of the FE phases accessible upon heating or cooling. Black arrows indicate regions where a particular phase is stable, and grey arrows indicate regions where the phase is metastable. Free energy curves are sketched on the right for selected temperatures (a, b, c and d).

the coefficients used to calculate $\epsilon_{11,T}$ were not optimized against any experimental permittivity data.

The difference between our predicted longitudinal relative permittivity with respect to experimental results as $T \rightarrow T_{CW,T}$ is likely the result of weak relaxor behavior, in agreement with Damjanovic [59]. Although the $T_{T-C} = 366$ K measured by Benabdallah *et al.* [51] was essentially frequency independent, a strong dispersion in the permittivity of the T phase and a relatively broad permittivity peak were observed. Additionally, see Figure 3, where a diffuse P-FE phase transition is observed as the spontaneous polarization decreases continuously to zero but exhibits a finite value at $T_{T-C} = 366$ K.

Further validation of the parameters was performed by estimating the longitudinal relative permittivity of an unpoled, polycrystalline BZT-50BCT sample using Equations (16a) and (16b) with $r_{90} = r_{71} = r_{109} = 1$ and comparing to experimental dielectric permittivity data from polycrystalline BZT-50BCT experiments measured at 1 kHz [37, 71–73], Figure 8. There is considerable variation in the experimental results, particularly at high temperatures. This variation could result from extrinsic effects related to porosity, grain size or unreported texture. Porosity and grain size varied across the experimental studies, where measured. For example, grain size and porosity were reported to be $5 \mu\text{m} - 10 \mu\text{m}$ and 9.8%, respectively, by Zhang [71] and $32 \pm 8 \mu\text{m}$ and 3%, respectively, by Brandt [72]. Texture effects are well-known: for tetragonal $\text{Ba}_{0.85}\text{Ca}_{0.15}\text{TiO}_3$ ceramics, the measured small-signal permittivity at $T < T_C$ decreases with increasing degree of (100) texture [27], and, similarly, for orthorhombic $\text{K}_{0.5}\text{Na}_{0.5}\text{NbiO}_3$ ceramics, (100) textured samples have lower dielectric permittivity than non-textured samples [74]. Unreported texture could contribute to the differences between experimental measurements and account for the overestimate of longitudinal

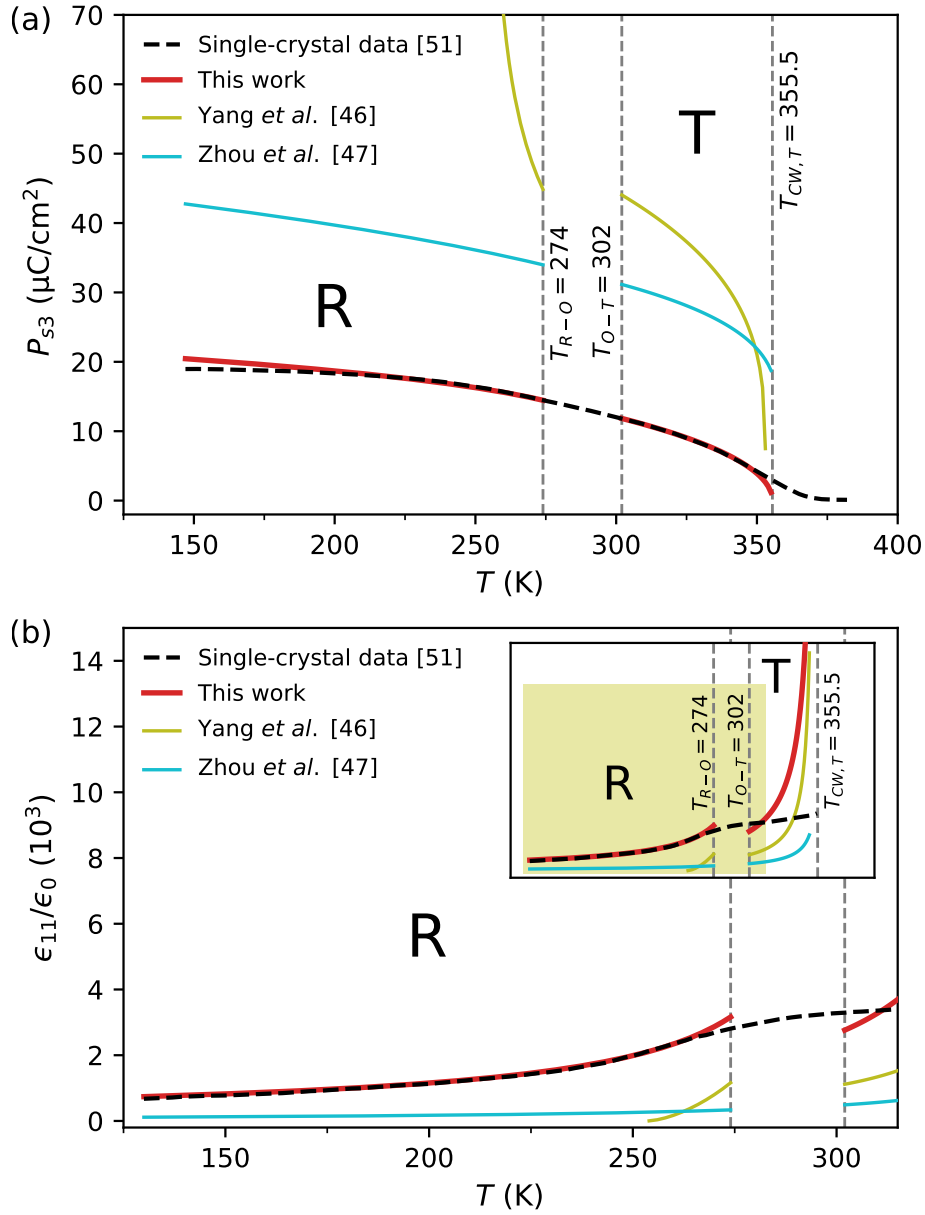


Figure 7. Comparison of predicted (a) P_{s3} vs T and (b) ϵ_{33}/ϵ_0 vs T to experimental measurements for single-crystal BZT-50BCT. Predictions from Yang *et al.* [46] and Zhou *et al.* [47] are also included for comparison. Experimental data for [001]-oriented BZT-50BCT single crystal are from Benabdallah *et al.* [51]. The transition temperatures T_{R-O} and T_{O-T} are from Ehmke [45]. $T_{CW,T}$ is the calculated Curie-Weiss temperature for the T phase in this work.

permittivity by our intrinsic, untextured polycrystalline prediction compared to the range of experimental data. Due to the lack of single-crystal experimental data, we used polycrystalline experimental results for validation, and, for expediency, we assumed that intrinsic behaviour dominated the polycrystalline response. A better way of validating against polycrystalline experimental results would be to simulate representative microstructures including extrinsic effects, but that was beyond the scope

of this work. Overall, the thermodynamic predictions for model intrinsic polycrystals in this work are consistent with experiments and validate the Landau coefficients optimized in this study for each FE phase.

Here, we employ macroscopic measured properties to optimize the Landau parameters in the FE-MPF model, and we implicitly assume that the experimentally observed phase is the thermodynamically stable phase at the temperature of interest. *Ab initio* phonon calculations and stability analyses would validate these assumptions or reveal other more stable states [75]. This approach was out-of-scope of the current study, but future *ab initio*-derived data should be utilised in parameter optimisation.

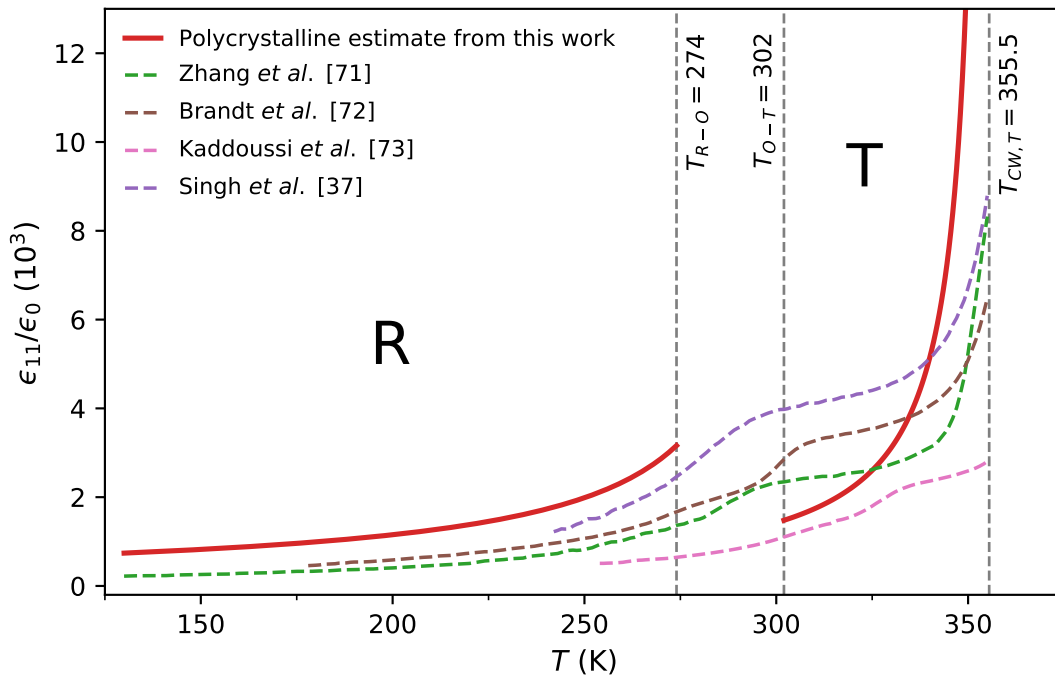


Figure 8. Comparison of predicted polycrystalline ϵ_{33}/ϵ_0 vs T to experimental data for unpoled polycrystalline BZT-50BCT ceramics. The transition temperatures T_{R-O} and T_{O-T} are from Ehmke [45]. $T_{CW,T}$ is the predicted Curie-Weiss temperature for the T phase in this work.

5. Conclusions

In this paper, we define a procedure to optimize single-crystal Landau parameters, compatible with, and inspired by, thermochemical parameter optimization processes established by the CALPHAD community. Best practice recommendations for CALPHAD include using a variety of measurement techniques to obtain properties, evaluating experimental sample preparation, not relying on phase stability alone to optimize parameters, documenting methodologies and data sets, and validating higher-order predictions against lower-order systems. Reevaluation of thermochemical data occurs episodically as new experimental or computational data becomes available and

propagates into the literature and available software. No such equivalent procedure exists in the ferroelectric research community. The coordinated data-driven analytics of sparse single-crystal and polycrystalline property measurements will enable the optimization of anisotropic single-crystal Landau coefficients to understand and engineer real ceramic systems by predicting optimal chemistries, processing and microstructures.

Here we demonstrate a formal parameter optimization procedure for ferroelectric ceramics by combining various single-crystal and polycrystalline experimental measurements related to the thermodynamic free energy function, rather than relying on phase boundaries alone, to optimize single-crystal Landau parameters. Phase boundaries and single-crystal and polycrystalline property measurements are used for validation. The assumptions in aggregating data from different researchers and how single-crystal data was estimated from polycrystalline measurements are reported, and the iterative, linear least squares optimization method is documented.

For the BZT-50BCT system, the optimization and validation are limited by the lack of single crystals of comparable composition and by the sparsity of property measurements in the literature [51]. To the best of the authors' knowledge, the optimized parameters correspond to the first set of experimentally-determined Landau coefficients reported for this system. These together with the FE-MPF model can be used in further research to predict properties and FE domain structures in single-crystal and polycrystalline BZT-50BCT samples enabling the identification of the mechanisms responsible for the enhanced electromechanical properties reported experimentally in the vicinity of interferroelectric transitions. With richer experimental data sets, uncertainties in experimental values could be quantified and incorporated in the parameter optimization. Further, modern parameter optimization methods, for example, genetic algorithms such as those used by Abolhasani *et al.* [23], will enable improved analyses.

Overall, the procedure proposed in this work can be readily extended to optimize the Landau and piezoelectric coefficients of the generality of FE systems using experimental data from polycrystalline samples in either saturated or unsaturated poling states. The remnant switching fractions of FE domains are required to use polycrystalline measurements to estimate the single-crystal properties, and can be obtained from XRD. The symmetry of the phases of interest determines the number of independent tensor coefficients and this, in turn, dictates the number of linearly independent property measurements that are required [61]. In this work, the FE phases are tetragonal and rhombohedral, which have the two lowest minimum number of independent tensor coefficients for ferroelectrics. Additional independent measurements are required to obtain orthorhombic or lower symmetry phase coefficients, which increases the burden on experimentalists. Our work illustrates the challenges of obtaining representative models of complex systems.

Acknowledgements

This work was supported by the University of Canterbury (College of Engineering PhD Scholarship). REG thanks the Erskine Fellowship, and the partial support from NSF grant 1734763. The authors thank M. C. Ehmke and J. E. Blendell for sharing their experimental data.

References

- [1] Bell A J 2008 *Journal of the European Ceramic Society* **28** 1307–1317
- [2] Rödel J, Jo W, Seifert K T P, Anton E M, Granzow T and Damjanovic D 2009 *Journal of the American Ceramic Society* **92** 1153–1177
- [3] Damjanovic D, Klein N, Li J and Porokhonsky V 2010 *Functional Materials Letters* **3** 5–13
- [4] Acosta M, Novak N, Rojas V, Patel S, Vaish R, Koruza J, Rossetti Jr G A and Rödel J 2017 *Applied Physics Reviews* **4** 041305
- [5] Gao J, Xue D, Liu W, Zhou C and Ren X 2017 *Actuators* **6** 24
- [6] Heitmann A A and Rossetti Jr G A 2014 *Journal of the American Ceramic Society* **97** 1661–1685
- [7] Acosta M, Khakpash N, Someya T, Novak N, Jo W, Nagata H, Rossetti G A and Rödel J 2015 *Physical Review B* **91** 104108
- [8] Ni Y and Khachaturyan A G 2012 *Acta Mechanica Solida Sinica* **25** 429–440
- [9] Rao W F and Wang Y U 2007 *Applied Physics Letters* **90** 182906
- [10] Liang L, Li Y L, Chen L Q, Hu S Y and Lu G H 2009 *Journal of Applied Physics* **106** 104118
- [11] Ma Z, Xi L, Liu H, Zheng F, Gao H, Chen Z and Chen H 2017 *Computational Materials Science* **135** 109–118
- [12] Wang Y L, Tagantsev A K, Damjanovic D, Setter N, Yarmarkin V K, Sokolov A I and Lukyanchuk I A 2007 *Journal of Applied Physics* **101** 104115
- [13] Callen H B 1985 *Thermodynamics and an Introduction to Thermostatistics* 2nd ed (New York: John Wiley)
- [14] Torres-Matheus O A, García R E and Bishop C M 2019 *Acta Materialia* **164** 577–585
- [15] Torres-Matheus O A, García R E and Bishop C M 2021 *Acta Materialia* **206** 116579 ISSN 1359-6454
- [16] Chen L Q 2007 APPENDIX A – Landau Free-Energy Coefficients *Physics of Ferroelectrics: A Modern Perspective (Topics in Applied Physics vol 105)* (Berlin, Heidelberg: Springer Berlin Heidelberg) pp 363–372 ISBN 978-3-540-34590-9
- [17] Tan X, Frederick J, Ma C, Aulbach E, Marsilius M, Hong W, Granzow T, Jo W and Rödel J 2010 *Physical Review B* **81** 014103
- [18] Zhao Z, Cao Y and García R E 2017 *Journal of the European Ceramic Society* **37** 573–581 ISSN 0955-2219
- [19] Zhang H, Lu X, Wang C, Zheng L, Yang B and Cao W 2018 *Physical Review B* **97** 054114
- [20] Zhang H, Lu X, Wang R, Wang C, Zheng L, Liu Z, Yang C, Zhang R, Yang B and Cao W 2017 *Physical Review B* **96** 054109
- [21] Heitmann A A and Rossetti Jr G A 2011 *Integrated Ferroelectrics* **126** 155–165 ISSN 1058-4587
- [22] Pitike K C, Khakpash N, Mangeri J, Rossetti G A and Nakhmanson S M 2019 *Journal of Materials Science* **54** 8381–8400 ISSN 1573-4803
- [23] Abolhasani M M, Zarejousheghani F, Cheng Z and Naebe M 2015 *RSC Advances* **5** 22471–22479 ISSN 2046-2069
- [24] Huang Q, Fan Z, Hong L, Cheng S, Tan Z, Tian G, Chen D, Hou Z, Qin M, Zeng M, Lu X, Zhou G, Gao X and Liu J M 2020 *Advanced Theory and Simulations* **3** 2000106 ISSN 2513-0390
- [25] Lukas H, Fries S G and Sundman B 2007 *Computational Thermodynamics: The Calphad Method* 1st ed (USA: Cambridge University Press) ISBN 978-0-521-86811-2

- [26] Ihlefeld J F, Harris D T, Keech R, Jones J L, Maria J P and Trolier-McKinstry S 2016 *Journal of the American Ceramic Society* **99** 2537–2557 ISSN 1551-2916
- [27] Schultheiß J, Clemens O, Zhukov S, von Seggern H, Sakamoto W and Koruza J 2017 *Journal of The American Ceramic Society* **100** 2098–2107
- [28] Lukas H L and Fries S G 1992 *Journal of Phase Equilibria* **13** 532–542 ISSN 1054-9714
- [29] Dovbenko O, Dreval L, Du Y, Liu Y, Liu S, Iljenko S and Effenberg G 2020 *Calphad* **68** 101719 ISSN 0364-5916
- [30] Kroupa A 2013 *Computational Materials Science* **66** 3–13 ISSN 0927-0256
- [31] Schmid-Fetzer R, Andersson D, Chevalier P Y, Eleno L, Fabrichnaya O, Kattner U R, Sundman B, Wang C, Watson A, Zabdyr L and Zinkevich M 2007 *Calphad* **31** 38–52 ISSN 0364-5916
- [32] Veber P, Benabdallah F, Liu H, Buse G, Josse M and Maglione M 2015 *Materials* **8** 7962–7978
- [33] Zeng Y, Zheng Y, Tu X, Lu Z and Shi E 2012 *Journal of Crystal Growth* **343** 17–20
- [34] Ehmke M C, Ehrlich S N, Blendell J E and Bowman K J 2012 *Journal of Applied Physics* **111** 124110
- [35] Sreenivas Puli V, Pradhan D K, Pérez W and Katiyar R 2013 *Journal of Physics and Chemistry of Solids* **74** 466–475
- [36] Sreenivas Puli V, Pradhan D K, Adireddy S, Martínez R, Silwal P, Scott J F, Ramana C V, Chrisey D B and Katiyar R S 2015 *Journal of Physics D* **48** 355502
- [37] Singh G, Sathe V and Tiwari V S 2017 *Journal of Electronic Materials* **46** 4976–4980
- [38] Gao J, Zhang L, Xue D, Kimoto T, Song M, Zhong L and Ren X 2014 *Journal of Applied Physics* **115** 054108
- [39] Haugen A B, Forrester J S, Damjanovic D, Li B, Bowman K J and Jones J L 2013 *Journal of Applied Physics* **113** 014103
- [40] Keeble D S, Benabdallah F, Thomas P A, Maglione M and Kreisel J 2013 *Applied Physics Letters* **102** 092903
- [41] Tian Y, Gong Y, Meng D, Deng H and Kuang B 2015 *Journal of Materials Science: Materials in Electronics* **26** 3750–3756
- [42] Zhang L, Zhang M, Wang L, Zhou C, Zhang Z, Yao Y, Zhang L, Xue D, Lou X and Ren X 2014 *Applied Physics Letters* **105** 162908
- [43] Damjanovic D, Biancoli A, Batooli L, Vahabzadeh A and Trodahl J 2012 *Applied Physics Letters* **100** 192907
- [44] Cordero F, Craciun F, Dinescu M, Scarisoreanu N, Galassi C, Schranz W and Soprunyuk V 2014 *Applied Physics Letters* **105** 232904
- [45] Ehmke M C 2014 *Ferroelastic Domains in Lead-Free Barium Zirconate Titanate - Barium Calcium Titanate Piezoceramics* Ph.D. thesis Purdue University
- [46] Yang T, Ke X and Wang Y 2016 *Scientific Reports* **6** 33392
- [47] Zhou C, Ke X, Yao Y, Yang S, Ji Y, Liu W, Yang Y, Zhang L, Hao Y, Ren S, Zhang L and Ren X 2018 *Applied Physics Letters* **112** 182903
- [48] Kabakov P, Dean C, Kurusingal V, Cheng Z, Lee H Y and Zhang S 2020 *Journal of Materials Chemistry C* **8** 7606–7649 ISSN 2050-7534
- [49] Liu D, Shim J, Sun Y, Li Q and Yan Q 2017 *AIP Advances* **7** 095311
- [50] Sun Y, Liu D, Li Q, Shim J, He W, Fang H and Yan Q 2018 *ACS Applied Materials & Interfaces* **10** 12847–12853 ISSN 1944-8244
- [51] Benabdallah F, Veber P, Prakasam M, Viraphong O, Shimamura K and Maglione M 2014 *Journal of Applied Physics* **115** 144102
- [52] Cao W 2004 *British Ceramic Transactions* **103** 71–75
- [53] Cao W 2008 *Ferroelectrics* **375** 28–39
- [54] Lines M E and Glass A M 2001 *Principles and Applications of Ferroelectrics and Related Materials* (Oxford: Oxford University Press)
- [55] Haun M J, Furman E, Jang S J, McKinstry H A and Cross L E 1987 *Journal of Applied Physics* **62** 3331–3338

- [56] Pérez J A, Soares M R, Paz F A A, Klinowski J, Senos A M R and Mantas P Q 2015 *Journal of Materials Science* **50** 4232–4243
- [57] Hou J, Wu Y and Wang Z 2015 *Computational Materials Science* **96** 327–335
- [58] Wu Y and Hou J 2014 *Journal of Applied Physics* **116** 114104
- [59] Damjanovic D 1998 *Reports on Progress in Physics* **61** 1267–1324
- [60] Li F X and Rajapakse R K N D 2007 *Journal of Applied Physics* **101** 054110
- [61] Nye J F 1957 *Physical Properties of Crystals: Their Representation by Tensors and Matrices* (Oxford: Clarendon Press)
- [62] Bowman K, Hoffman M and Jones J 2005 *Journal of Applied Physics* **98** 024115–024115
- [63] Ryo H S and Ryo I G 2016 *Applied Physics A* **122** 745
- [64] Lu W, Fang D N, Li C Q and Hwang K C 1999 *Acta Materialia* **47** 2913–2926
- [65] Yang F, Wu Y, Li H and Jiang J 2010 *Ferroelectrics* **408** 62–70
- [66] Hill R 1963 *Journal of the Mechanics and Physics of Solids* **11** 357–372
- [67] Li F X, Zhou X L and Soh A K 2010 *Applied Physics Letters* **96** 152905
- [68] Newville M, Stensitzki T, Allen D B and Ingargiola A 2014 LMFIT: Non-linear least-square minimization and curve-fitting for python Zenodo
- [69] Bell A J and Cross L E 1984 *Ferroelectrics* **59** 197–203
- [70] Smolenskii G A, Isupov V A, Ktitorov S A, Trepakov V A and Yushin N K 1979 *Soviet Physics Journal [translation of Izvestiya Vysshikh Uchebnykh Zavedenii, Fizika]* **22** 3–30
- [71] Zhang L, Ren X and Carpenter M A 2017 *Physical Review B* **95** 054116
- [72] Brandt D R J, Acosta M, Koruza J and Webber K G 2014 *Journal of Applied Physics* **115** 204107
- [73] Kaddoussi H, Lahmar A, Gagou Y, Manoun B, Chotard J N, Dellis J L, Kutnjak Z, Khemakhem H, Elouadi B and El Marssi M 2017 *Journal of Alloys and Compounds* **713** 164–179
- [74] Haugen A B, Morozov M I, Jones J L and Einarsrud M A 2014 *Journal of Applied Physics* **116** 214101
- [75] Sadok R B, Hammoutène D and Plugaru N 2021 *physica status solidi (b)* **258** 2000289 ISSN 1521-3951